JACS
JOURNAL OF THE AMERICAN CHEMICAL SOCIETY
pubs.acs.org/JACS
Article

Localized 4f Magnetism and Low-Lying 5d-Mediated Photoresponses in Layered TmI_2

Hao Ni, Mingyang Yuan, Lin-Ke Li, Zhe Wang, Lili Zhao, Zhengwei Fu, Yue Zhao, Song Bao, Weigao Xu, Zhaobo Hu,* Qiuxiang Wang, Jinsheng Wen, Shuang Chen,* and Ningxin Jiang*

Cite This: J. Am. Chem. Soc. 2026, 148, 49310−49323
Read Online
ACCESS | Metrics & More | Article Recommendations | Supporting Information

ABSTRACT: Divalent rare-earth solids with a $4f^{n+1}$ configuration provide access to electronic structures in which localized 4f states coexist with low-lying, structurally responsive 5d states, yet the combined magnetic, electrical, and optical manifestations of these states remain underexplored in extended Tm^{2+} compounds. Here, we investigate layered TmI_2 as an extended Tm^{2+} solid and employ Cs_4TmI_6 with isolated TmI_6 units and dilute SrI_2:Tm^{2+} as targeted reference systems. Structural, spectroscopic, and X-ray photoelectron spectroscopic measurements support Tm^{2+} as the dominant oxidation state, while electronic-structure calculations reveal narrow, localized, occupied Tm 4f-derived bands and low-lying Tm 5d-derived unoccupied states, with substantially greater 5d dispersion in TmI_2 than in Cs_4TmI_6. Magnetic measurements establish localized $4f^{13}$ Kramers-ion behavior on the triangular Tm^{2+} lattice of TmI_2, together with a small negative low-temperature Weiss temperature and no evidence of long-range magnetic ordering down to 2 K. Comparative luminescence, photothermal, and photocurrent measurements reveal distinct photoresponses across the three systems within a shared electronic-level framework encompassing 4f−5d and 4f−4f transitions. Relative to Cs_4TmI_6 and SrI_2:Tm^{2+}, TmI_2 exhibits a lower-energy optical absorption onset, weaker photoluminescence, and a more pronounced light-induced current response despite its high electrical resistivity. Its wavelength-dependent photothermal response broadly follows the 4f−5d absorption profile. Together, these results establish layered TmI_2 as a distinctive rare-earth platform that combines the $4f^{13}$ magnetic characteristics familiar from Yb^{3+} systems with low-energy 4f−5d excitations, expanding the scope for investigating rare-earth magnetic solids with optical excitation channels beyond 4f−4f transitions.

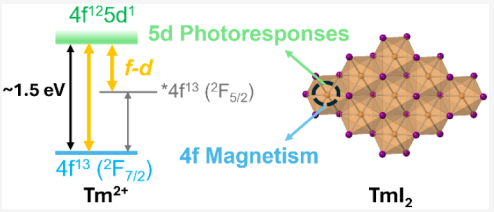

1. INTRODUCTION

Rare-earth (RE) elements combine localized electronic states, strong spin−orbit coupling, and chemically tunable coordination environments, giving rise to diverse optical, magnetic, and electronic properties. In most RE compounds, the trivalent oxidation state dominates, and the resulting $4f^n$ configurations have been widely exploited in phosphors, ceramics, quantum materials, and energy-related solids.[1−7] Unusual RE valence states, however, provide access to electronic structures and physical responses that extend beyond those commonly encountered in RE^{3+} chemistry. Recent advances in high-valent RE compounds have revealed unusual bonding, redox chemistry, catalytic reactivity, and magnetic behavior.[8−13] Low-valent RE chemistry represents a complementary frontier, in which reduction alters both the electron count and the relative energies of the 4f and 5d manifolds.

Divalent RE chemistry has historically been dominated by the comparatively stable Sm^{2+}, Eu^{2+}, and Yb^{2+} ions.[14] Early studies also identified a number of halides and chalcogenides with less readily stabilized RE^{2+} and established their crystal structures and preliminary physical properties.[15,16] More recently, molecular RE^{2+} chemistry has expanded across nearly the entire RE series, revealing new opportunities in magnetism and small-molecule activation.[17−21] By contrast, extended solids containing RE^{2+} ions beyond Sm^{2+}, Eu^{2+} and Yb^{2+} remain comparatively underexplored, particularly with respect to the relationship between lattice connectivity, electronic structure, and physical responses.[22]

Compared with RE^{3+}, divalent RE systems generally exhibit reduced 4f−5d energy separation.[23] While the 4f orbitals remain highly localized and effectively shielded, the spatially more extended 5d orbitals are strongly influenced by coordination geometry, crystal-field effects, and metal−ligand interactions. In extended RE^{2+} solids, low-lying 5d-derived states may additionally acquire appreciable dispersion and participate in excitation migration, nonradiative relaxation, or charge transport.

Within divalent RE chemistry, Sm^{2+}, Eu^{2+}, Tm^{2+}, and Yb^{2+} are commonly classified as traditional divalent ions with $4f^{n+1}$ configurations, in contrast to the $4f^n5d^1$ configurations in nontraditional RE^{2+} systems. Among the former, Tm^{2+} offers a

Received: July 23, 2026
Revised: November 2, 2026
Accepted: November 3, 2026
Published: November 6, 2026

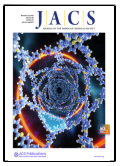

ACS Publications
© 2026 American Chemical Society

https://doi.org/10.1021/jacs.6c15247
J. Am. Chem. Soc. 2026, 148, 49310−49323

Downloaded from pubs.acs.org/jacsat/article-pdf/148/45/49310/6911201 8/jacs.6c15247.pdf by NANJING UNIV user on 19 November 2026

particularly compelling combination of magnetic and optical characteristics, yet their combined manifestations in extended solids remain comparatively underexplored.[24−27] Tm^{2+} adopts a $4f^{13}$ electronic configuration and is isoelectronic with Yb^{3+}, a well-established Kramers ion in near-infrared-emitting and quantum magnetic materials.[28−30] The $4f^{13}$ configuration supports characteristic intraconfigurational 4f−4f transitions between the $^2F_{7/2}$ and $^2F_{5/2}$ multiplets, while low-lying $4f^{12}5d^1$ excited states give rise to broad 4f−5d absorption extending into the visible and near-infrared regions in halide environments.

This combination distinguishes Tm^{2+} from the more extensively studied divalent ions. Unlike Sm^{2+} and Yb^{2+}, whose $4f^6$ and $4f^{14}$ configurations have J = 0 ground states, Tm^{2+} supports a Kramers local moment. Compared with the $4f^7$, L = 0 ground state of Eu^{2+}, Tm^{2+} provides an orbitally active $4f^{13}$ ground multiplet together with a near-infrared 4f−4f transition and low-energy access to an environment-sensitive 5d manifold (Figure 1). A well-separated ground-state Kramers doublet can further support an effective spin-1/2 description at sufficiently low temperatures, motivating exploration of Tm^{2+} in geometrically frustrated lattices. Layered TmI_2 is particularly well suited for investigating this combination because its edge-sharing TmI_6 octahedra form an extended Tm−I framework and a crystallographically regular triangular arrangement of Tm^{2+} ions.

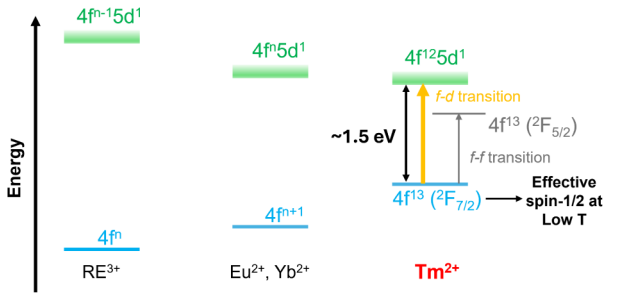

Figure 1. Schematic comparison of the 4f and 5d-related energy levels of RE^{3+} ions, selected RE^{2+} ions, and Tm^{2+}. The Tm^{2+} level separations approximately reflect the experimentally observed optical transition energies, whereas the diagram as a whole is not drawn to scale and does not imply absolute energy alignment between columns. Excited states within the 4f configurations of the reference ions and detailed crystal-field splittings are omitted for clarity. The green bands represent 5d-containing excited-state manifolds, and the arrows indicate optical excitations.

Here, we investigate layered TmI_2 as an extended Tm^{2+} solid and employ Cs_4TmI_6 with isolated TmI_6 octahedra and Tm^{2+}-doped SrI_2 (SrI_2:Tm^{2+}) with dilute, seven-coordinate Tm^{2+} centers as complementary references. By combining structural, spectroscopic and valence-state characterizations and electronic-structure calculations, we establish a comparative picture of Tm^{2+}-based iodides featuring localized 4f states and low-lying, structurally responsive 5d states. The localized $4f^{13}$ configuration supports characteristic near-infrared 4f−4f transitions and Kramers-ion magnetic behavior, while the environment-sensitive 5d-derived states provide access to broad visible−near-infrared absorption. Comparative measurements reveal distinct luminescence, photothermal, and photocurrent responses within this electronic-level framework, encompassing both 4f−4f and 4f−5d transitions. In layered TmI_2, low-energy optical absorption coexists with high electrical resistivity and a reproducible light-induced current response, highlighting the combination of localized magnetism and optical responsiveness accessible in an extended RE^{2+} compound.

2. RESULTS AND DISCUSSION

2.1. Sample Preparation and Structural Characterization

TmI_2 and SrI_2:Tm^{2+} were prepared using modified literature procedures, whereas Cs_4TmI_6 was synthesized using a strategy analogous to that reported for the structurally related Rb_4TmI_6.[26,31,32] Detailed synthetic procedures are provided in the Experimental Section of the Supporting Information. To protect the highly air- and moisture-sensitive products, the starting materials were sealed in arc-welded niobium tubes and subsequently enclosed in evacuated quartz ampules (Figure S1). TmI_2 single crystals were obtained by heating a mixture of TmI_3 and Tm metal to 780 °C followed by slow cooling (Figure S2). Prolonged reaction of Tm metal with TmI_3 at 550 °C afforded TmI_2 as a brown powder, denoted TmI_2-p, in higher yield, although a minor TmOI impurity was detected by PXRD (Figure S4). Unless otherwise specified, TmI_2 characterizations were performed using selected single crystals or powders obtained by grinding these crystals. TmI_2-p was used for wavelength-dependent photocurrent and photothermal measurements. To assess the influence of sample preparation on the light-induced electrical response, pellets prepared from TmI_2-p and powder obtained by grinding selected TmI_2 single crystals were compared under identical 808 nm irradiation conditions. Both preparations exhibited reproducible light-induced current responses with similar light-to-dark current ratios, despite differences in their absolute currents (Figure S33). Single-crystal X-ray diffraction (SCXRD) analyses were performed on crystals of TmI_2 and Cs_4TmI_6. SrI_2:Tm^{2+}, which served as a dilute reference, was prepared with a nominal Tm^{2+} concentration of 9.0 mol % on the divalent-cation sublattice. Detailed synthetic procedures are provided in the Supporting Information.

TmI_2 adopts the CdI_2-type layered structure in the trigonal space group ($P\bar{3}m1$) (Figure 2a−c). The Tm^{2+} ions form a crystallographically perfect two-dimensional triangular lattice, and each Tm^{2+} center is coordinated by six iodide ions in an approximately octahedral environment, with six equivalent Tm−I distances of 3.146(2) Å. Each iodide ligand adopts a μ_3-bridging coordination mode and connects three neighboring Tm centers, generating extended layers of edge-sharing $[TmI_6]^{4-}$ octahedra. The shortest intralayer Tm···Tm distance is 4.507(1) Å, whereas the separation between adjacent Tm-containing layers is 6.943(3) Å.

Cs_4TmI_6 crystallizes in the $R\bar{3}c$ space group and exhibits structural features similar to those of the previously reported Rb_4TmI_6 analogue (Figure 2d, e). Its structure contains discrete $[TmI_6]^{4-}$ octahedra that are spatially separated by Cs^+ cations, with no direct connectivity between neighboring $[TmI_6]^{4-}$ units. The Tm−I distance in Cs_4TmI_6 is 3.1653(3) Å, slightly longer than that in TmI_2, whereas the shortest Tm···Tm distance increases substantially to 8.8768(2) Å. Thus, Cs_4TmI_6 represents a stoichiometric but structurally isolated zero-dimensional Tm−I connectivity among the Tm^{2+} iodides examined here.

The Tm−I distances in TmI_2 and Cs_4TmI_6 are appreciably longer than the 2.988(3) Å distance reported for crystalline TmI_3.[33] Although direct bond-length comparisons are also

Downloaded from pubs.acs.org/jacsat/article-pdf/148/45/49310/6911201 8/jacs.6c15247.pdf by NANJING UNIV user on 19 November 2026

https://doi.org/10.1021/jacs.6c15247
J. Am. Chem. Soc. 2026, 148, 49310−49323

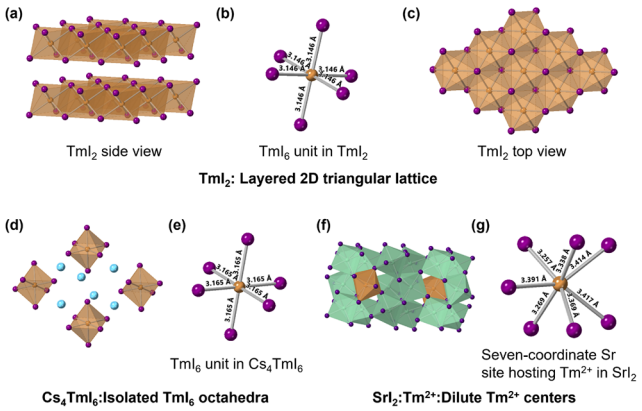

Figure 2. Crystal structures and local coordination environments of TmI_2, Cs_4TmI_6, and SrI_2:Tm^{2+}. (a) Side view of the layered TmI_2 structure. (b) Six-coordinate TmI_6 unit in TmI_2, with Tm−I bond lengths indicated. (c) Top view of a TmI_2 layer, showing the triangular arrangement of Tm centers within the edge-sharing octahedral network. (d) Isolated TmI_6 octahedra in Cs_4TmI_6 and (e) the corresponding local coordination environment, with Tm−I bond lengths indicated. (f) Schematic distribution of dilute Tm^{2+} centers within the SrI_2 host framework. (g) Seven-coordinate Sr site hosting Tm^{2+}, with Sr−I distances taken from the host structure. Panels (a−e) are based on the single-crystal structures of TmI_2 and Cs_4TmI_6, whereas panels (f, g) use the SrI_2 host structure; the highlighted Tm sites are illustrative and do not imply an ordered dopant arrangement. Purple spheres represent I atoms, orange-brown spheres and polyhedra highlight Tm centers and their coordination environments, blue spheres represent Cs atoms, and green polyhedra represent Sr−I coordination units. All distances are given in Å.

influenced by coordination geometry, the observed elongations of approximately 0.16−0.18 Å are consistent with the larger effective ionic radius expected upon reduction from Tm^{3+} ($4f^{12}$) to Tm^{2+} ($4f^{13}$) and with analogous bond-length expansions observed in molecular Tm^{2+} complexes.[34] These structural features support the assignment of divalent Tm in TmI_2 and Cs_4TmI_6.

Rietveld refinements were performed using powder X-ray diffraction (PXRD) data collected for powders obtained by grinding selected TmI_2 single crystals and powder obtained by grinding the entire Cs_4TmI_6 reaction product (Figure 3a, b). The principal diffraction peak positions of TmI_2 agree with those calculated from the single-crystal structural model, with no detectable reflections attributable to TmOI or other impurity phases. However, the (001) reflection near 2θ = 12.5° exhibits splitting, while pronounced broadening is observed in the region of the (002) and (011) reflections near 25.5° and 25.97°, respectively. These features suggest structural heterogeneity involving the interlayer periodicity, potentially associated with stacking disorder along the *c* axis. Stacking-related modifications of diffraction profiles have also been reported for other layered compounds.[35,36] To describe the observed peak splitting, an approximate model comprising two TmI_2 components with slightly different unit-cell parameters was employed, yielding a lower R_{wp} than the single-component refinement (Figures 3a and S5). This model provides an empirical description of the diffraction profile rather than a unique determination of the underlying disorder.

In comparison, refinement of the directly synthesized TmI_2-p sample, including its minor TmOI impurity, yielded an R_{wp} of 10.2% (Figure S5). The differences between the diffraction profiles suggest that the structural heterogeneity may depend

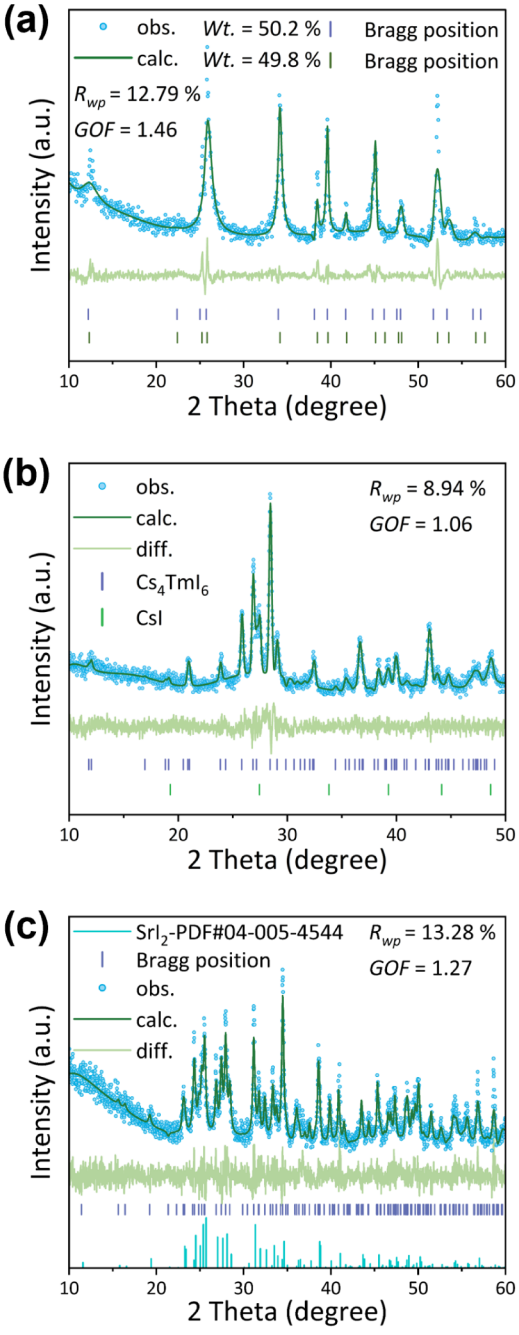

Figure 3. Powder X-ray diffraction patterns and Rietveld refinements of (a) TmI_2, (b) Cs_4TmI_6, and (c) SrI_2:Tm^{2+}. Observed, calculated, and difference profiles are shown together with the corresponding Bragg reflection positions. For (a), the refinement employs two TmI_2 components with slightly different unit-cell parameters to account for the observed peak splitting. Bragg tick marks indicate the reflections of the components included in each refinement, including minor secondary phases where present. The reference diffraction pattern of SrI_2 is also shown in (c).

on the synthesis and crystal-growth conditions. Cs_4TmI_6 was obtained as the predominant crystalline phase, together with approximately 3 wt % residual CsI. Inductively coupled plasma optical emission spectroscopy (ICP-OES) showed that the bulk Tm contents of both samples were close to their calculated values, further supporting the assigned compositions of the principal phases (Table S4).

Downloaded from pubs.acs.org/jacsat/article-pdf/148/45/49310/6911201 8/jacs.6c15247.pdf by NANJING UNIV user on 19 November 2026

https://doi.org/10.1021/jacs.6c15247
J. Am. Chem. Soc. 2026, 148, 49310−49323

The PXRD pattern of SrI_2:Tm^{2+} closely matched that of the orthorhombic SrI_2 host, with no detectable reflections from crystalline TmI_2 or other secondary phases (Figure 3c). Rietveld refinement using the SrI_2 structural model, with the Sr site modeled as 91% Sr and 9% Tm, provided good agreement with the experimental pattern. Energy-dispersive X-ray spectroscopy additionally showed a homogeneous spatial distribution of Sr and Tm across the examined particles (Figure S6). These results are consistent with retention of the SrI_2 host structure and a homogeneous distribution of incorporated Tm at the microscale.[31] ICP-OES gave a bulk Tm fraction of x = 0.090, defined as x = Tm/(Sr + Tm), in good agreement with the nominal value of 9.0%.

The local coordination environments of the Tm sites were compared across the three samples (Figure 2). In both TmI_2 and Cs_4TmI_6, Tm^{2+} is coordinated by six iodide ions at equivalent distances, forming slightly distorted octahedral environments with D_{3d} and S_6 site symmetries, respectively. The I−Tm−I angles are approximately 88.5° and 91.5° in TmI_2, compared with 89.9° and 90.1° in Cs_4TmI_6, indicating that the latter more closely approaches ideal octahedral geometry. In contrast, the Sr site hosting Tm^{2+} in orthorhombic SrI_2 is seven-coordinate and has C_1 site symmetry. Differences in coordination number, geometry, and local symmetry can modify crystal-field splittings and optical transition intensities, particularly for the spatially extended 5d states, and therefore provide an additional basis for interpreting the spectral differences among these compounds.

2.2. Electronic Structure Characterization

UV−vis−NIR diffuse-reflectance spectroscopy was employed to further probe the electronic configurations of the Tm centers. Spectra were collected over the range of 250−1400 nm for the three Tm^{2+}-containing samples and for a TmI_3 reference (Figure 4). The TmI_3 reference exhibits a series of relatively weak and narrow absorption bands at approximately 476, 704, 806, 1205, and 1230 nm (2.605, 1.761, 1.538, 1.029, and 1.008 eV, respectively), characteristic of parity-forbidden intraconfigurational 4f−4f transitions of Tm^{3+}.[37] By contrast, the spectra of the Tm^{2+}-containing iodides are dominated by broad absorption features extending from the ultraviolet through the visible into the near-infrared region, consistent with parity-allowed interconfigurational $4f^{13} \rightarrow 4f^{12}5d^1$ transitions characteristic of divalent RE ions.[38]

A weaker but well-resolved narrow absorption band is observed near 1138 nm (1.089 eV) for all three Tm^{2+}-containing samples. This feature is assigned to the intraconfigurational $4f^{13}\,{}^2F_{7/2} \rightarrow 4f^{13}\,{}^2F_{5/2}$ transition of Tm^{2+}.[39] By comparison, no distinct absorption attributable to the characteristic Tm^{3+} 4f−4f transition near 1200 nm was detected above the spectral background. These observations support the assignment of Tm as predominantly divalent in TmI_2, Cs_4TmI_6, and SrI_2:Tm^{2+}.

Within the broad 4f → 5d absorption envelope, two principal components can be resolved between approximately 550 and 900 nm for each Tm^{2+}-containing sample. These occur at approximately 760 and 657 nm (1.631 and 1.887 eV) in TmI_2 and at 730 and 624 nm (1.698 and 1.987 eV) in Cs_4TmI_6. In SrI_2:Tm^{2+}, a shoulder near 742 nm (1.671 eV) accompanies the band centered at 642 nm (1.931 eV). The corresponding energy separations are approximately 0.256, 0.289, and 0.260 eV, respectively. These low-energy absorption features fall within the range reported for 4f→5d transitions in other Tm^{2+}-containing halides, supporting the present assignment.[23,31] These bands are tentatively assigned to transitions from the $4f^{13}\,{}^2F_{7/2}$ ground manifold to the lowest crystal-field-split $4f^{12}({}^3H_6)5d^1$ excited states.[23] Exchange coupling between the 5d electron and the $4f^{12}$ core further separates these excited configurations into high-spin and low-spin components. The lower-energy high-spin component is nominally spin-forbidden from the $4f^{13}$ ground state, whereas the higher-energy low-spin component is spin-allowed. In the spectra of TmI_2 and Cs_4TmI_6, the two components exhibit more comparable spectral intensities than in dilute SrI_2:Tm^{2+}, for which the intensity contrast between the two bands is more pronounced. This difference may reflect variations in crystal-field splitting, local symmetry, and electronic-state mixing, which can modify the relative oscillator strengths of the nominally spin-allowed and spin-forbidden transitions. At higher energies, additional maxima occur at 534 and 467 nm (2.322 and 2.655 eV) in TmI_2 and at 521 and 456 nm (2.380 and 2.719 eV) in Cs_4TmI_6, whereas SrI_2:Tm^{2+} exhibits a shoulder near 524 nm (2.366 eV) and a maximum at 460 nm (2.695 eV). The higher-energy absorption region likely contains contributions from multiple $4f^{12}5d^1$ excited states and is therefore not further deconvoluted.

The spectra also illustrate the different environmental sensitivities of the 4f- and 5d-derived states. The narrow $4f^{13}\,{}^2F_{7/2} \rightarrow {}^2F_{5/2}$ absorption remains centered near 1138 nm in all three Tm^{2+}-containing samples, consistent with the

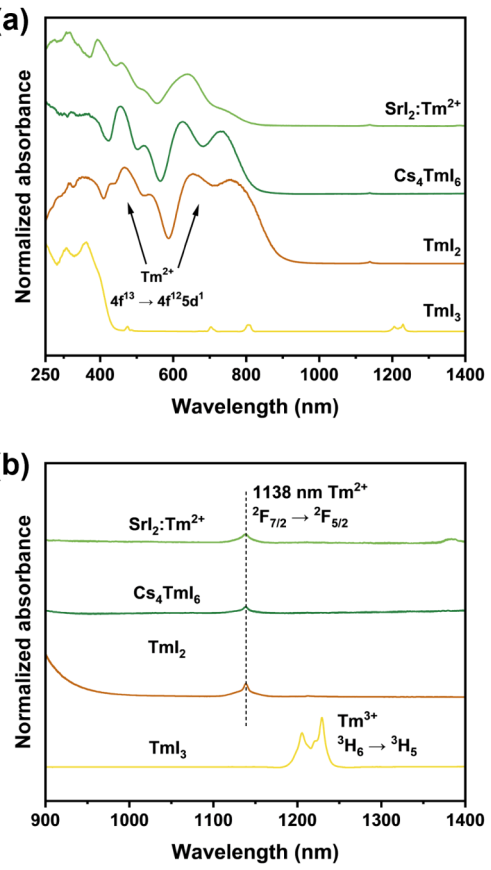

Figure 4. UV−vis−NIR diffuse-reflectance spectra of thulium iodides. (a) Normalized absorption spectra of TmI_3, TmI_2, Cs_4TmI_6, and SrI_2:Tm^{2+} from 250 to 1400 nm. (b) Expanded near-infrared region from 900 to 1400 nm. Spectra are vertically offset for clarity.

https://doi.org/10.1021/jacs.6c15247
J. Am. Chem. Soc. 2026, 148, 49310−49323

Downloaded from pubs.acs.org/jacsat/article-pdf/148/45/49310/6911201 8/jacs.6c15247.pdf by NANJING UNIV user on 19 November 2026

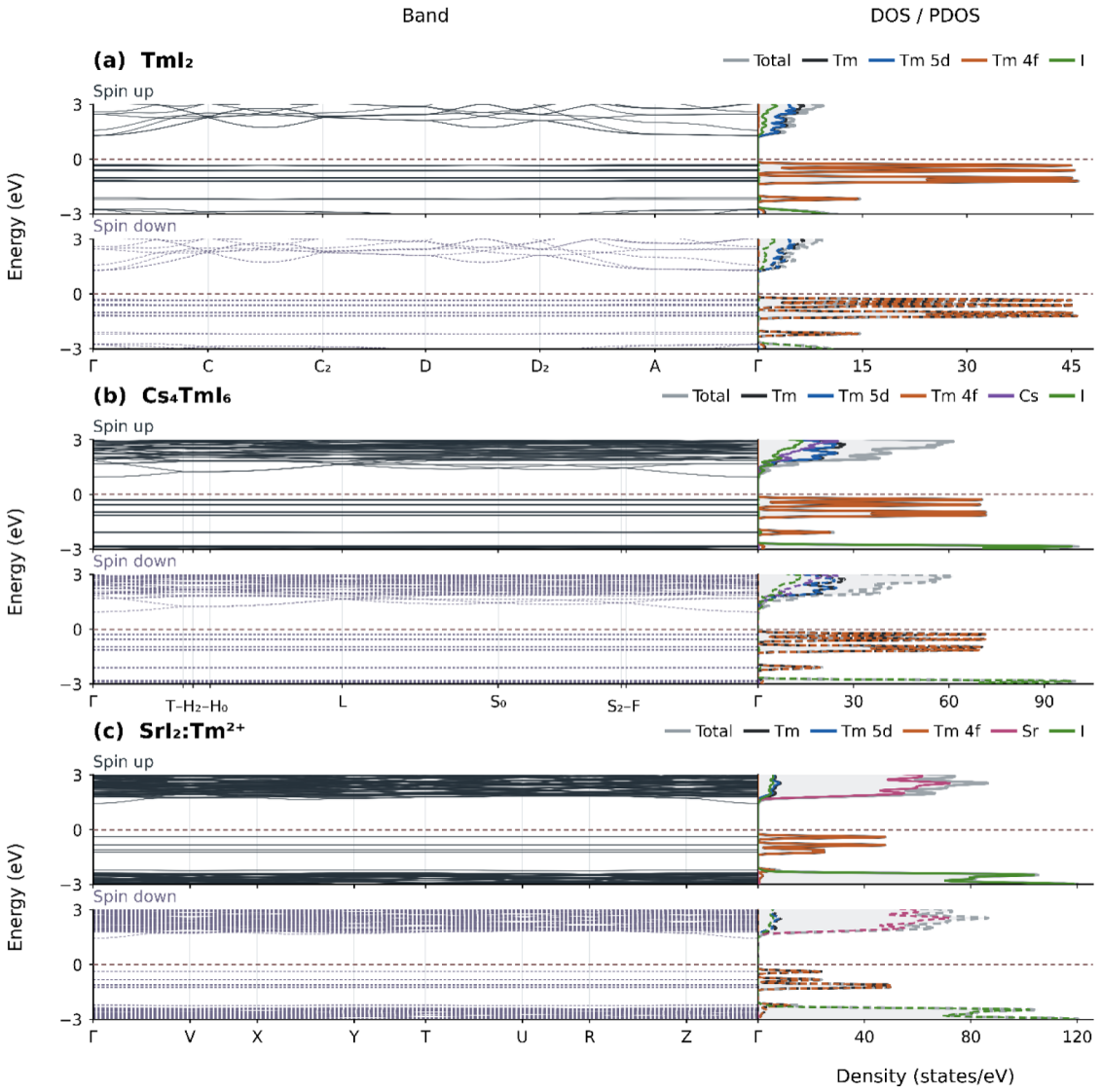

Figure 5. Spin-polarized electronic structures of (a) TmI_2, (b) Cs_4TmI_6, and (c) SrI_2:Tm^{2+} (9 mol %). Left panels show the band structures along the indicated high-symmetry k-paths; right panels display the total and projected densities of states (TDOS/PDOS). Spin-up and spin-down channels are plotted in the upper and lower halves of each panel, respectively. The Fermi level is set to 0 eV, and the plotted energy window is −3 to +3 eV. The projected contributions of Tm, Sr, Cs, and I orbitals, together with the separately resolved Tm 5d and Tm 4f states, are color-coded as indicated in the legends.

effective shielding and localized character of the 4f orbitals. By contrast, the broad 4f → 5d absorption bands vary substantially in position and line shape across the series, reflecting the greater sensitivity of the spatially extended 5d orbitals to coordination geometry, ligand field, and lattice connectivity. The lowest-energy 4f → 5d component in TmI_2 is shifted to lower energy by approximately 0.067 eV relative to Cs_4TmI_6 and 0.040 eV relative to the shoulder in SrI_2:Tm^{2+}. The second component exhibits corresponding shifts of approximately 0.100 and 0.044 eV. These shifts are tentatively ascribed to enhanced stabilization of the 5d-derived states in the structurally connected TmI_2 lattice, potentially aided by greater electronic delocalization or dispersion. However, differences in local coordination and site symmetry also contribute to these transition energies, precluding attribution of the shifts solely to lattice connectivity.

For an empirical comparison of the selected absorption-edge regions, the Kubelka−Munk-transformed spectra were additionally analyzed using Tauc plots with a direct-transition model (Figure S7). Because the low-energy absorption in the Tm^{2+}-containing compounds contains substantial contributions from localized or partially localized 4f → 5d excitations, the extracted values should not be interpreted as conventional intrinsic semiconductor band gaps. Rather, they are treated as apparent optical transition energies that provide an empirical comparison of the selected absorption-edge regions. The apparent transition energies obtained for TmI_2, Cs_4TmI_6, and SrI_2:Tm^{2+} are 1.45, 1.56, and 1.76 eV, respectively, whereas TmI_3 exhibits a substantially larger value of 3.00 eV.[40] The low-energy absorption of the Tm^{2+}-containing samples is consistent with the presence of low-lying 5d-derived excited states.

X-ray photoelectron spectroscopy provided complementary evidence for the divalent character of Tm in TmI_2 (Figures S9−S14). Relative to TmI_3, the Tm 4d spectrum of TmI_2 exhibits an additional lower-binding-energy feature at 171.5

Downloaded from pubs.acs.org/jacsat/article-pdf/148/45/49310/6911201 8/jacs.6c15247.pdf by NANJING UNIV user on 19 November 2026

https://doi.org/10.1021/jacs.6c15247
J. Am. Chem. Soc. 2026, 148, 49310−49323

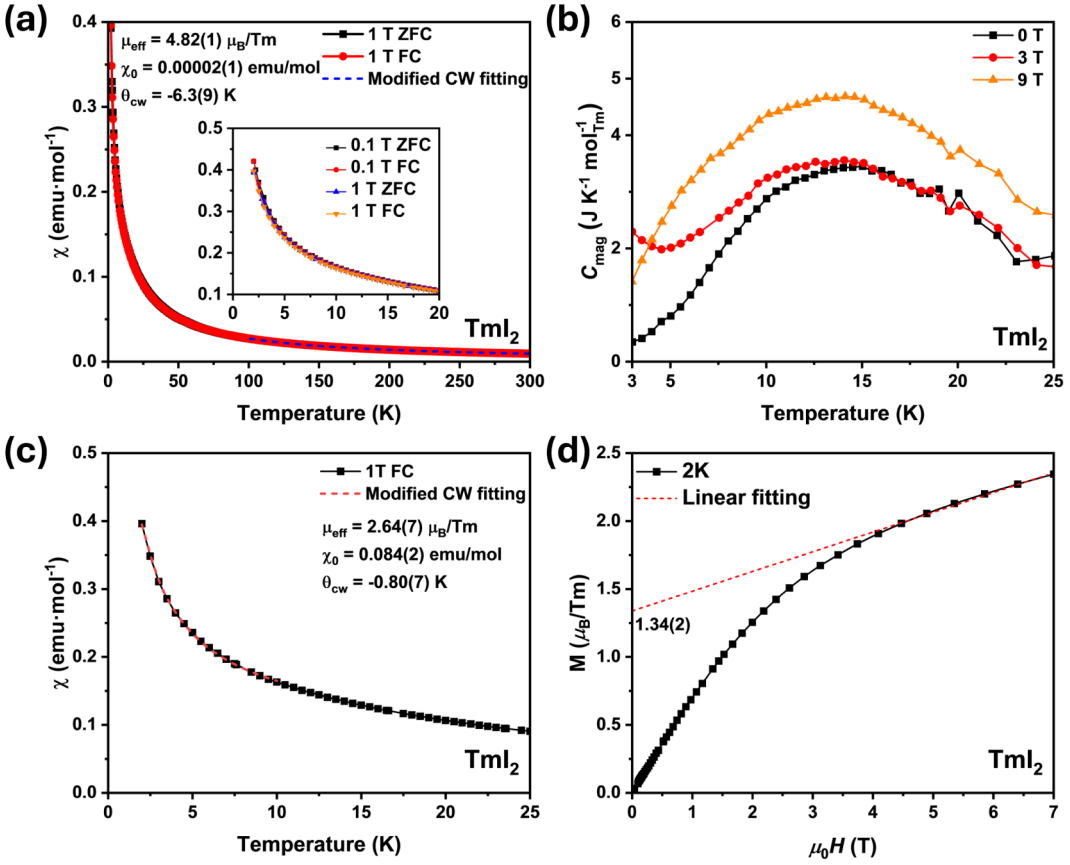

Figure 6. Magnetic properties of TmI_2. (a) Temperature-dependent molar magnetic susceptibility of TmI_2 measured under 1 T under both FC and ZFC conditions from 2 to 300 K; the blue dashed curve shows the modified Curie−Weiss fit. Inset: low-temperature FC and ZFC susceptibilities of TmI_2 measured under 0.1 and 1 T from 2 to 20 K. (b) Magnetic heat capacity of TmI_2 obtained after subtraction of lattice contribution from 3 to 25 K under 0, 3, and 9 T. The lattice contribution was estimated and subtracted using heat-capacity data of YbI_2. (c) Low-temperature FC molar magnetic susceptibility of TmI_2 measured under 1 T from 2 to 25 K, together with the modified Curie−Weiss fit. (d) Field-dependent magnetization of TmI_2 measured at 2 K from 0 to 7 T. The red dashed line shows a linear fit to the high-field data, extrapolated to zero field; its intercept is 1.34(2) μB per Tm.

eV, consistent with the characteristic response of $4f^{13}$ Tm^{2+} compounds (Figure S10a).[41] An analogous shift toward lower binding energy was observed between YbI_3 and YbI_2 measured under identical conditions, supporting the assignment (Figure S10b).[42] Higher-binding-energy Tm^{3+}-like components in TmI_2 are tentatively attributed mainly to partial surface oxidation; their intensities are therefore not used to quantify the bulk Tm^{3+} fraction. Ar^+ sputter depth profiling was additionally performed to assess the contribution of surface oxidation (Figure S11). Following sputtering, lower-binding-energy features near 172 eV were observed in both TmI_3 and TmI_2. Their appearance in the TmI_3 reference suggests sputtering-induced changes in surface speciation, potentially involving reduction, analogous to the formation of metallic Pb following Ar^+ irradiation of $MAPbI_3$.[43] Consequently, the sputtered spectra were not used to establish the intrinsic Tm oxidation-state distribution. In addition, the valence spectra show further evidence for RE^{2+} in both TmI_2 and YbI_2 as detailed in the Supporting Information. Taken together, the crystallographic data, characteristic Tm^{2+} absorption features, and XPS results consistently support Tm^{2+} as the dominant bulk oxidation state in TmI_2.

2.3. Band Structure Calculation Based on DFT

To gain further insight into the electronic structures of TmI_2, Cs_4TmI_6, and SrI_2:Tm^{2+} (9 mol %) and to provide a computational framework for interpreting their optical and semiconducting properties, density functional theory (DFT) calculations were performed on three model compounds. The calculated spin-polarized band structures and projected density of states (PDOS), with the spin-up and spin-down channels resolved separately, are shown in Figure 5. The Fermi level is set to 0 eV for each compound.

The calculated electronic structures reveal that all three compounds possess similar band structures and frontier states with both the spin-up and spin-down channels derived primarily from Tm- and I-based orbitals, but that the connectivity of the $[TmI_6]^{4-}$ octahedra strongly influences the dispersion and spatial character of these states. In all three compounds, the upper valence bands just below the Fermi level are extremely narrow and nearly dispersionless, consistent with their dominant contribution from highly localized Tm 4f orbitals. For TmI_2 and Cs_4TmI_6, the low-lying conduction bands are primarily derived from Tm 5d orbitals and I 5p orbitals. In the case of SrI_2:Tm^{2+}, the Tm concentration is highly diluted, so that the low-lying conduction bands in both spin channels are primarily derived from Sr s orbitals, with additional contributions from Tm 5d and I 5p orbitals. Compared with the two-dimensional Tm−I network in TmI_2, the structurally isolated $[TmI_6]^{4-}$ units in Cs_4TmI_6 exhibit less dispersive Tm 5d-derived conduction states, consistent with

Downloaded from pubs.acs.org/jacsat/article-pdf/148/45/49310/6911201 8/jacs.6c15247.pdf by NANJING UNIV user on 19 November 2026

https://doi.org/10.1021/jacs.6c15247
J. Am. Chem. Soc. 2026, 148, 49310−49323

greater spatial localization. SrI_2:Tm^{2+} provides a complementary dilute reference with a distinct seven-coordinate environment and predominantly host-derived low-lying conduction states. Similar calculation results have been reported recently on $CsTmX_3$ compounds.[44]

The calculated direct gaps of TmI_2, Cs_4TmI_6, and SrI_2:Tm^{2+} are 1.58, 1.22, and 1.82 eV, respectively, which agree with the experimentally observed visible-near-infrared absorption edges. These Kohn−Sham gaps are smaller than the experimentally extracted apparent optical transition energies for Cs_4TmI_6, yet the agreement is relatively good for the studied systems involving localized f-electrons and spin-polarized states. The small deviation primarily reflects the intrinsic limitation of the semilocal exchange−correlation functional, rather than any significant physical discrepancy. Notably, the Cs-derived contribution to the conduction band is negligible, whereas I 5p states also contribute alongside Tm 5d states. The optical spectra are more appropriately compared with the energy separation between the occupied Tm 4f-derived states and the low-lying Tm 5d-projected unoccupied states, which captures the structural sensitivity of the Tm^{2+} 5d manifold more directly. Thus, the calculations reliably identify the orbital character of the frontier bands and the effect of $[TmI_6]^{4-}$ connectivity, providing a physically consistent description of the optical properties. Additional spin-polarized calculations on magnetic properties were also performed for three compounds (Figure S15), as discussed in detail below and in the Supporting Information.

Overall, the calculated electronic structures support a picture in which the localized $4f^{13}$ manifold defines the occupied frontier states and underlies the ion-centered magnetic behavior and near-infrared 4f−4f spectroscopic features, whereas the more spatially extended Tm 5d-derived states provide low-energy accepting states for broad 4f → 5d optical excitation. The presence of these low-lying 5d-derived states distinguishes these Tm^{2+} iodides from many trivalent RE systems dominated by low-energy 4f − 4f excitations and provides an electronic-structure framework for interpreting the magnetic and optical responses discussed below.

2.4. Localized 4f Magnetism in Layered TmI_2

In recent years, two-dimensional $4f^{13}$ Yb^{3+} magnets, such as $YbMgGaO_4$ and $NaYbO_2$,[29,30,45,46] have attracted considerable attention as triangular-lattice frustrated magnets and quantum spin-liquid candidates. Tm^{2+} is isoelectronic with Yb^{3+} and possesses a $4f^{13}$ configuration, yet its solid-state magnetic behavior remains much less explored. Previous studies have largely been limited to a small number of molecular Tm^{2+} magnets and valence-variable thulium chalcogenides, including TmCh (Ch = S, Se, and Te).[47−49] We therefore investigated the magnetic properties and temperature- and field-dependent heat capacity of TmI_2, using Cs_4TmI_6 and SrI_2:Tm^{2+} as magnetic reference systems containing structurally isolated and dilute Tm^{2+} centers, respectively, to assess the roles of single-ion effects and interionic interactions.

Temperature-dependent molar magnetic susceptibilities were collected between 2 and 300 K under applied fields of 0.1 and 1 T using both zero-field-cooling (ZFC) and field-cooling (FC) conditions (Figures 6a and S16). For TmI_2, Cs_4TmI_6, and SrI_2:Tm^{2+}, the susceptibility increases monotonically upon cooling, with no clear signature of long-range magnetic ordering or a magnetic phase transition within the measured temperature range. Consistently, the magnetic heat capacity of TmI_2 (Figure 6b) shows no sharp λ-type anomaly down to 3 K under 0, 3, and 9 T, providing no evidence for a long-range magnetic ordering transition within this temperature range. The field-dependent magnetization curves collected at 2 K show no pronounced magnetic hysteresis within the experimental resolution (Figure S17a).

Curie−Weiss analysis was performed using the 1 T FC susceptibility of TmI_2 (Figure 6a). The high-temperature data were analyzed with a modified Curie−Weiss expression, $\chi_m = \chi_0 + C/(T - \theta_{CW})$, where χ_0 accounts for temperature-independent contributions. Fitting over the 100−300 K range gives an apparent effective moment of $\mu_{eff} = 4.82(1)\ \mu_B$ per Tm, with a Weiss temperature of $\theta_{CW} = -6.3(9)$ K. This effective moment is much closer to the free-ion value expected for $4f^{13}$ Tm^{2+}, $\mu_{eff} = 4.54\ \mu_B$, than to that of $4f^{12}$ Tm^{3+}, $\mu_{eff} = 7.56\ \mu_B$, supporting the assignment of Tm^{2+} as the dominant magnetic species.

For a $4f^{13}$ ion, the $^2F_{7/2}$ ground multiplet is split by the crystal field into four Kramers doublets. At sufficiently low temperature, thermal depopulation of the excited doublets can lead to magnetic behavior dominated by the lowest Kramers doublet, analogous to the effective spin-1/2 description often used for Yb^{3+} magnets. To probe this regime, the low-temperature susceptibility of TmI_2 was further analyzed between 2 and 10 K (Figure 6c). A modified Curie−Weiss fit in this range yields a reduced apparent effective moment of 2.64(7) μ_B per Tm, with a Weiss temperature of −0.80(7) K. In addition, the 2 K magnetization curves of TmI_2 bend toward saturation at moderate fields (Figure 6d), followed by a weak high-field linear contribution. After subtracting this high-field linear contribution, the magnetization of TmI_2 approaches approximately 1.34(2) μ_B per Tm. This value is close to one-half of the reduced effective moment obtained from the low-temperature modified Curie−Weiss fit. A similar magnitude of powder-averaged saturation magnetization has been reported for Yb^{3+}-based frustrated magnets, consistent with the response of anisotropic ground-state Kramers doublets.[50,51] These observations are consistent with a crystal-field-split Tm^{2+} manifold in which the low-temperature magnetism is governed primarily by the lowest Kramers doublet.

A comparison among TmI_2, Cs_4TmI_6 and SrI_2:Tm^{2+} further provides insight into the origin of their magnetic behavior (Figures 6, S18−S23). The three compounds exhibit broadly comparable magnetic responses, including comparable high-temperature apparent effective moments, negative Weiss temperatures, reduced low-temperature moments, and similar 2 K field-dependent magnetization curves despite their different structures, local symmetries and Tm^{2+} concentrations. The temperature-dependent effective moments of all three samples are also presented in the Supporting Information (Figure S17b). This similarity suggests that the measured magnetic response within the accessible temperature and field ranges is dominated primarily by the local single-ion magnetism of iodide-coordinated Tm^{2+} centers. The small magnitudes of the low-temperature Weiss temperatures are compatible with this interpretation, but their negative signs alone do not uniquely distinguish exchange interactions from single-ion contributions. The present measurements therefore provide no direct evidence for collective magnetic correlations in TmI_2, while leaving open the possibility that such correlations emerge at lower temperatures.

The magnetic heat capacity of TmI_2 provides further insight into its low-temperature magnetic behavior (Figure 6b). The

Downloaded from pubs.acs.org/jacsat/article-pdf/148/45/49310/6911201 8/jacs.6c15247.pdf by NANJING UNIV user on 19 November 2026

https://doi.org/10.1021/jacs.6c15247
J. Am. Chem. Soc. 2026, 148, 49310−49323

lattice contribution was estimated using the nonmagnetic $4f^{14}$ compound YbI_2, with a scaling factor determined by matching the heat capacities above 40 K (Figure S24). After subtraction, C_{mag} exhibits a broad maximum around 10−15 K rather than a sharp λ-type anomaly. This feature is consistent with thermal population of low-lying crystal-field excited doublets within the $Tm^{2+2}F_{7/2}$ manifold, although a unique crystal-field level scheme cannot be established from the present data. The field-induced low-temperature upturn is consistent with a Schottky contribution associated with Zeeman splitting of the ground-state Kramers doublet. Integration of C_{mag}/T from 3 to 40 K yields recovered magnetic entropies of approximately 4.78 and 8.25 $J{\cdot}K^{-1}{\cdot}mol^{-1}$ at 0 and 9 T, respectively (Figure S25). These values represent entropy changes within the measured temperature window and exclude contributions below 3 K. The larger recovered entropy at 9 T is consistent with a field-induced redistribution of magnetic entropy into this window. The recovered entropy at 9 T exceeds R ln 2, consistent with contributions from excited crystal-field doublets in addition to the ground-state doublet over the 3−40 K interval, although its precise magnitude depends on the estimated lattice background. Taken together, the heat-capacity and magnetization results support a predominantly single-ion interpretation involving crystal-field excitations and Zeeman splitting over the measured range.

Additional spin-polarized DFT calculations described in the Supporting Information provide a qualitative computational comparison with the magnetic measurements (Figure S15). For TmI_2, Cs_4TmI_6, and SrI_2:Tm^{2+}, antiferromagnetically aligned spin configurations are calculated to be energetically favored over the corresponding ferromagnetic configurations, indicating an energetic preference for antiferromagnetic alignment within the models examined. This result is qualitatively consistent with the negative Weiss temperatures and suggests a tendency toward antiferromagnetic coupling.

Overall, the predominantly single-ion magnetic response is consistent with the highly localized character of the Tm 4f electrons and the small apparent interaction scale inferred from the low-temperature susceptibility. The available measurements establish TmI_2 as a triangular-lattice Tm^{2+} magnet with a low-temperature Kramers-doublet response and a small negative Weiss temperature consistent with weak net antiferromagnetic interactions. No evidence of long-range magnetic ordering is observed down to 2 K. These measurement limits remain above the scale suggested by $|\theta_{CW}| \approx 0.8$ K, so the absence of ordering does not by itself demonstrate frustration-induced suppression of a magnetic transition. Nevertheless, weak interactions do not preclude unconventional behavior at substantially lower temperatures. For example, the triangular-lattice Yb^{3+} compound $KBaYb(BO_3)_2$ exhibits a small Weiss temperature of approximately −0.06 K and no detected long-range order or spin freezing down to 50 mK, motivating consideration of a possible quantum spin-liquid ground state.[52,53] This precedent highlights the importance of probing temperatures at and below the relevant interaction scale. Although the present data do not establish collective magnetic correlations or a quantum-disordered ground state in TmI_2, the combination of Kramers local moments, triangular geometry, and an antiferromagnetic coupling tendency identifies it as a promising platform for further subkelvin quantum magnetic and thermodynamic studies.[54] More broadly, Tm^{2+} provides an isoelectronic analogue of Yb^{3+} with distinct valence, ionic size, and coordination chemistry, extending the search for rare-earth quantum magnets to divalent halide frameworks.

2.5. Electrical Transport in TmI_2

The highly localized nature of RE 4f orbitals generally limits their contribution to dispersive electronic bands, whereas the more spatially extended 5d orbitals can participate more effectively in band formation and charge transport. In many trivalent RE solids, the 5d-derived states lie at relatively high energy, limiting their accessibility for low-energy excitation and transport.[55] Reduction to the divalent state can stabilize the 5d manifold and narrow the 4f−5d energy separation, providing access to lower-energy electronic excitations and, in some cases, narrow-gap semiconducting behavior. EuO is a representative divalent RE ferromagnetic semiconductor in which localized 4f moments coexist with low-lying 5d-derived electronic states.[27] Motivated by the layered structure of TmI_2, its relatively low apparent optical transition energy, and the semiconducting electronic structure predicted by DFT calculations, we investigated its temperature-dependent electrical transport in the dark (Figure 7).

The room-temperature resistivity of a pressed TmI_2 pellet prepared from ground single crystals was first measured using the van der Pauw method. At 298 K, the effective resistivity

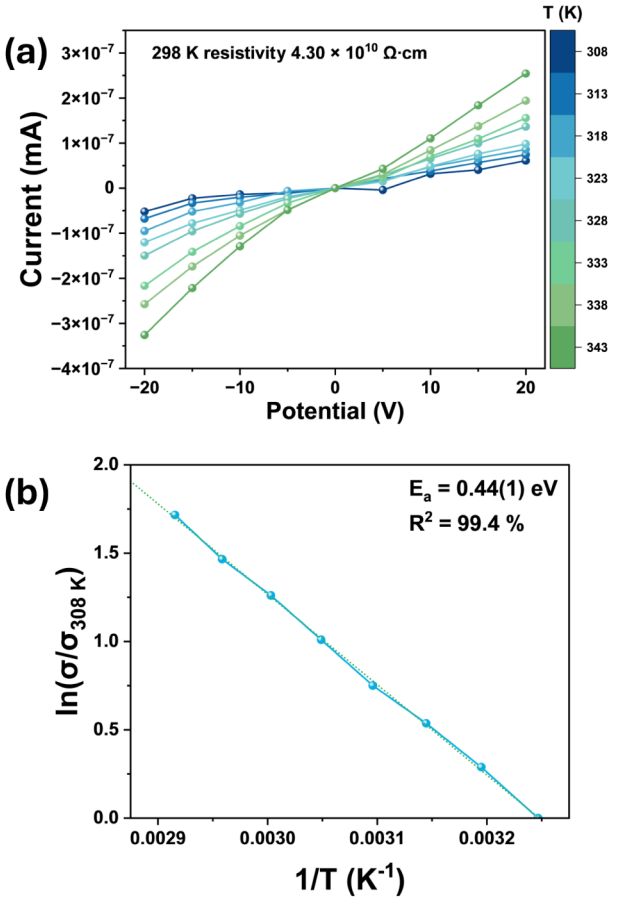

Figure 7. Dark electrical transport of a pressed TmI_2 pellet prepared from ground single crystals. (a) Temperature-dependent I−V curves from 308 to 343 K. (b) Arrhenius analysis of the temperature-dependent relative conductivity of TmI_2. The dashed line represents the linear fit based on the Arrhenius equation, $\sigma = \sigma_0 \exp\left(-\frac{E_a}{k_B T}\right)$. The solid line is included as a guide to the eye.

Downloaded from pubs.acs.org/jacsat/article-pdf/148/45/49310/6911201 8/jacs.6c15247.pdf by NANJING UNIV user on 19 November 2026

https://doi.org/10.1021/jacs.6c15247
J. Am. Chem. Soc. 2026, 148, 49310−49323

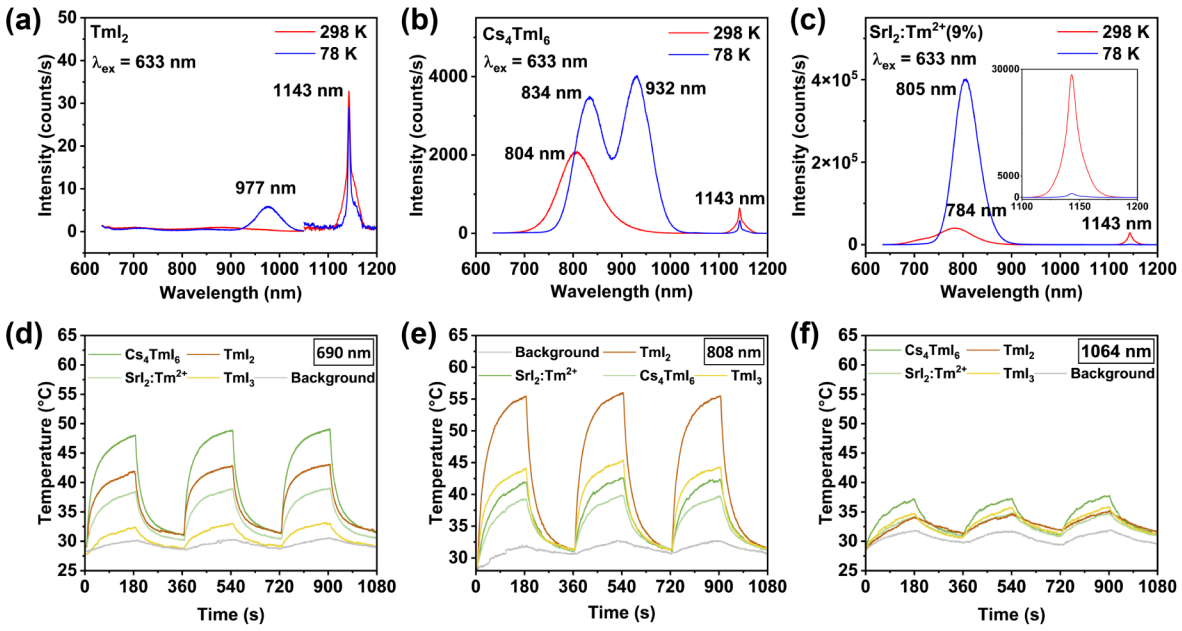

Figure 8. Photoluminescence and photoinduced heating of thulium iodides. (a–c) Photoluminescence spectra of (a) TmI_2, (b) Cs_4TmI_6, and (c) SrI_2:Tm^{2+} at 298 and 78 K under 632.8 nm excitation. Intensities are displayed in counts/s without normalization to individual peak maxima; note the different vertical scales. The inset in (c) expands the narrow emission near 1143 nm at both temperatures. (d–f) Apparent surface temperature profiles of TmI_2-p, Cs_4TmI_6, SrI_2:Tm^{2+}, and TmI_3 under repeated laser on/off cycles at (d) 690 nm, (e) 808 nm, and (f) 1064 nm, with an incident power density of 1 W·cm^{-2}. Measurements were performed using a quartz-window-protected configuration. Gray curves show the background measurements described in the Supporting Information.

was 4.30×10^{10} Ω·cm, indicating that TmI_2 is a highly resistive material rather than a good electrical conductor. To assess whether this high resistivity primarily reflects the use of a pressed pellet, a selected TmI_2 single crystal was additionally measured using a two-probe configuration with copper contacts at its two ends (Figure S26). At 298 K, the measured resistance was 3.68×10^{11} Ω, corresponding to an estimated resistivity of approximately 2.0×10^{10} Ω·cm based on the crystal dimensions. Although the two-probe value includes contact contributions and uncertainty associated with the crystal geometry, the high resistance observed in the single crystal suggests that the highly resistive response is not solely a consequence of pellet grain boundaries. The calculated electronic structure indicates that the upper valence states are dominated by localized Tm 4f orbitals, whose limited dispersion may restrict transport involving these states and contribute to the high measured resistivity, although carrier mobility was not independently determined.

The pellet resistance decreased monotonically with increasing temperature. This negative temperature coefficient is consistent with thermally activated electrical transport. An Arrhenius analysis over the measured temperature range yielded an apparent activation energy of approximately 0.44(1) eV. This value characterizes the measured transport process and is not directly equated with the optical transition energy.

2.6. 5d-Mediated Photoresponses in TmI_2

Tm^{2+} combines a $4f^{13}\ ^2F_{7/2}$ ground multiplet with a low-lying $4f^{13}\ ^2F_{5/2}$ excited multiplet and accessible $4f^{12}5d^1$ excited-state manifolds, providing both near-infrared 4f–4f and broad visible–near-infrared 4f–5d optical transitions in the iodides studied here. This combination extends beyond the predominantly 4f–4f-based low-energy optical response of many RE^{3+} systems and differs from Eu^{2+} and Yb^{2+}, which lack an analogous low-energy intraconfigurational 4f–4f transition. Whereas the localized 4f states provide relatively environment-insensitive spectroscopic signatures, the spatially extended 5d states offer excitation channels sensitive to local coordination and lattice connectivity. We therefore compare the photoluminescence, photothermal, and light-induced electrical responses of TmI_2, Cs_4TmI_6, and SrI_2:Tm^{2+} to examine how these distinct structural environments influence their photoresponses.

2.6.1. Photoluminescence of Tm^{2+}-Containing Iodides. Yb^{3+}, which is isoelectronic with Tm^{2+}, is widely used as a near-infrared luminescent ion because of its characteristic $4f^{13}\ ^2F_{5/2} \rightarrow\ ^2F_{7/2}$ transition.[28] To examine these radiative channels and their dependence on the structural environment, photoluminescence spectra were collected at 298 and 78 K under 632.8 nm excitation for TmI_2, Cs_4TmI_6, and SrI_2:Tm^{2+} (Figure 8a–c).

Under the measurement conditions employed, TmI_2 exhibits substantially weaker detected photoluminescence than Cs_4TmI_6 and SrI_2:Tm^{2+}, but its emission remains clearly resolvable. A narrow band near 1143 nm (1.085 eV) is observed in TmI_2 at both temperatures, while cooling reveals an additional weak broad band centered near 977 nm (1.269 eV). Cs_4TmI_6 exhibits a broad maximum at 804 nm (1.542 eV) at 298 K; at 78 K, two broad maxima are resolved at 834 and 932 nm (1.487 and 1.330 eV). A weaker narrow feature near 1143 nm is also observed at both temperatures. In SrI_2:Tm^{2+}, the broad emission shifts from 784 nm (1.581 eV) at 298 K to 805 nm (1.540 eV) at 78 K and increases markedly in peak intensity upon cooling. The narrow emission near 1143 nm decreases substantially upon cooling but remains resolvable in the expanded spectrum (Figure 8c, inset). Despite its much lower intensity relative to the broad 805 nm band, its detected peak intensity at 78 K remains higher than those of the

Downloaded from pubs.acs.org/jacsat/article-pdf/148/45/49310/6911201 8/jacs.6c15247.pdf by NANJING UNIV user on 19 November 2026

https://doi.org/10.1021/jacs.6c15247
J. Am. Chem. Soc. 2026, 148, 49310–49323

corresponding emissions in TmI_2 and Cs_4TmI_6. The spectra retain the measured intensity scales rather than being normalized to individual maxima; nevertheless, these detected intensities should not be equated with photoluminescence quantum yields.

The narrow emission near 1143 nm is assigned to the intraconfigurational $4f^{13}\ ^2F_{5/2} \rightarrow {}^2F_{7/2}$ transition, whereas the broad bands are tentatively assigned to $4f^{12}5d^1 \rightarrow 4f^{13}$ emission. At 78 K, the 977 nm band of TmI_2 lies approximately 0.27 eV below the 805 nm band of SrI_2:Tm^{2+}, while the two broad components of Cs_4TmI_6 are separated by approximately 0.16 eV. These variations contrast with the nearly unchanged position of the narrow 4f−4f band and are consistent with the greater sensitivity of the 5d-containing excited states to coordination geometry, local symmetry, and excited-state relaxation. The excitation spectrum of SrI_2:Tm^{2+} monitored near 1140 nm additionally follows the broad 4f−5d absorption features (Figure S27), supporting population of the emitting $4f^{13}\ ^2F_{5/2}$ manifold following 4f−5d excitation. Its temperature-dependent emission qualitatively resembles that reported for SrI_2 containing approximately 7% Tm^{2+}, where cooling favors broad 5d−4f emission relative to the narrow 4f−4f band.[31]

The two broad bands observed in Cs_4TmI_6 at 78 K suggest contributions from distinct emitting states within the $4f^{12}5d^1$ manifold. Multiple-state emission involving high-spin- and low-spin-related states has been reported in other Tm^{2+}-doped halides, providing a possible framework for interpreting this behavior.[23] Time-resolved photoluminescence (TRPL) measurements yield fitted decay times of approximately 37 ns at 298 K and 29 ns at 78 K, monitored at 810 and 830 nm, respectively (Figure S28). These wavelengths sample the broad emission near 804 and 834 nm in the corresponding steady-state spectra. The results establish a fast decay component at both temperatures, with a modest shortening upon cooling. Although this change accompanies the emergence of the 932 nm band, the present data do not establish population transfer between the two emission components or uniquely determine their high-spin or low-spin character. In particular, the measured decay times include both radiative and nonradiative contributions. TRPL measurements were not performed on TmI_2 because its weak photoluminescence intensity precluded reliable decay measurements with the available setup. A reliable lifetime for the approximately 800 nm emission of SrI_2:Tm^{2+} could not be extracted within the accessible temporal window of the present setup. For comparison, Plokker et al. reported a lifetime of approximately 265 μs at 20 K for the 821 nm emission of SrI_2 containing 7.2% Tm^{2+}.[31] This lifetime remained approximately constant up to 100 K and decreased to approximately 11 μs at 300 K. These values provide a relevant reference time scale for the corresponding broad emission observed in our SrI_2:Tm^{2+} sample and suggest substantially slower decay than the nanosecond-scale dynamics measured for Cs_4TmI_6. Due to the temporal limitations of the present experimental setup, the 1 MHz repetition rate of the excitation source restricts the accessible temporal window to approximately 1 μs.

The observed emission features are consistent with the 5d−4f and 4f−4f transitions reported for Tm^{2+} halides. However, transient Tm^{3+} formation following excitation cannot be excluded, given the precedent of reversible photoinduced valence changes in Eu/Dy-doped phosphors, and would require further investigation by valence-sensitive spectroscopy under controlled illumination.[56]

Together, these measurements show that iodide-coordinated Tm^{2+} centers support both 4f−4f and 5d−4f radiative channels, with pronounced differences in detected intensity, spectral profile, and temperature dependence across the three structural environments. Although the specific contributions of lattice connectivity, Tm^{2+} concentration, and defects to the weak emission of TmI_2 remain unresolved, its coexistence with broad 4f−5d absorption motivates direct investigation of photoinduced heating, as discussed below.

2.6.2. Wavelength-Dependent Photothermal Response. To examine photoinduced heating associated with the broad optical absorption of the Tm^{2+}-containing iodides, photoinduced-heating measurements were performed on TmI_2-p, Cs_4TmI_6, SrI_2:Tm^{2+}, and TmI_3 under identical quartz-window-protected conditions (Figures 8d−f, S31 and S32). The TmI_2-p sample used for these measurements was the directly synthesized powder described in Section 2.1.

Under 690 nm irradiation, all three Tm^{2+}-containing samples exhibited larger apparent surface-temperature increases than TmI_3. Under 808 nm irradiation, TmI_2 showed the most pronounced heating response, followed by TmI_3, whereas Cs_4TmI_6 and SrI_2:Tm^{2+} exhibited smaller temperature increases. The appreciable response of TmI_3 at 808 nm is consistent with its observed 4f−4f absorption band near 806 nm. By contrast, excitation at 1064 nm produced only weak heating for all samples.

Photothermal conversion under 808 nm excitation has previously been investigated in Tm^{3+}-based materials.[57,58] In comparison, the Tm^{2+}-containing iodides exhibit broad 4f−5d absorption encompassing both 690 and 808 nm and show photoinduced heating at both wavelengths. This wavelength dependence broadly follows the absorption profiles and illustrates the potential of low-lying 5d-derived states to broaden the excitation window for thulium-based photothermal responses beyond individual 4f−4f absorption bands.

However, the measured temperature increases depend on absorbed optical power, sample heat capacity, and heat exchange with the surroundings. Differences in composition, density, pellet packing, and thermal contact can therefore affect the results even under matched irradiation and nominal sample geometry. Accordingly, these measurements characterize specimen-level heating under the experimental conditions used and do not establish an intrinsic photothermal conversion efficiency ranking or a per-ion comparison of Tm^{2+} and Tm^{3+}. Detailed experimental data and discussion are provided in the Supporting Information.

2.6.3. Wavelength-Dependent Photoconductive Response of TmI_2. To examine the photoconductive response of TmI_2, current−time measurements were performed using a previously established two-probe configuration (Figure 9).[59] The wavelength-dependent measurements presented here were conducted using TmI_2-p. A comparison with powder obtained by grinding TmI_2 single crystals showed similar light-to-dark current ratios under 808 nm irradiation, despite differences in their absolute dark currents (Figure S33).

At applied biases between 1 and 10 V, irradiation at 808 nm with an incident power density of 0.5 $W{\cdot}cm^{-2}$ produced a reproducible increase in current. At 10 V, the current increased from a dark value of approximately 4×10^{-11} A to 2.4×10^{-10} A under illumination, corresponding to a light-to-dark current ratio of approximately 6. Repeated laser on/off cycles produced clearly resolved current increases followed by

Downloaded from pubs.acs.org/jacsat/article-pdf/148/45/49310/6911201 8/jacs.6c15247.pdf by NANJING UNIV user on 19 November 2026

https://doi.org/10.1021/jacs.6c15247
J. Am. Chem. Soc. 2026, 148, 49310−49323

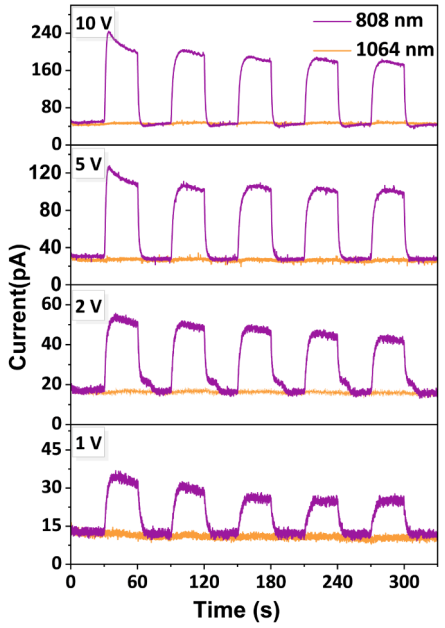

Figure 9. Current−time traces of TmI_2-p under periodic 808 and 1064 nm laser illumination at applied biases of 10, 5, 2, and 1 V, from top to bottom. The incident laser power density was 0.5 $W{\cdot}cm^{-2}$.

recovery toward the dark baseline, although some variation in response amplitude was observed.

For comparison, analogous measurements were performed on Cs_4TmI_6 and SrI_2:Tm^{2+} under 808 nm irradiation (Figure S34). Both reference samples exhibited low dark currents, with no clearly resolved light-induced current modulation above the background fluctuations, even at an applied bias of 10 V. These results establish a pronounced contrast between TmI_2 and the structurally isolated or dilute Tm^{2+} reference systems under the measurement conditions used. This contrast is consistent with a role for the extended Tm−I framework in supporting a measurable light-induced electrical response, although differences in resistivity, local coordination, and electrical contacts preclude attribution solely to lattice connectivity.

A substantially weaker response was observed under 1064 nm irradiation. At 10 V and the same incident power density, the current increased by only approximately 16% relative to the corresponding dark value (Figure S35). The photon energies at 808 and 1064 nm are approximately 1.53 and 1.17 eV, respectively. The 808 nm excitation lies within the pronounced low-energy $4f^{13} \rightarrow 4f^{12}5d^1$ absorption envelope of TmI_2, whereas absorption at 1064 nm is substantially weaker. The stronger electrical response at 808 nm is therefore consistent with the wavelength dependence of the optical absorption.

The current enhancement cannot be assigned exclusively to direct photoconductivity because TmI_2 exhibits strongly thermally activated dark transport and simultaneous photoinduced heating. The relative contributions of photocarrier generation, thermally assisted transport, and contact effects remain unresolved. Nevertheless, the reproducible light-induced current, together with the thermally activated dark transport discussed above, supports semiconductor-like electrical behavior in this highly resistive Tm^{2+} solid.

2.7. Localized 4f Magnetism and 5d-Mediated Photoresponses in Layered TmI_2

Layered TmI_2 extends the chemistry of triangular-lattice $4f^{13}$ magnets from familiar Yb^{3+} systems to a divalent halide framework. The magnetic measurements support predominantly single-ion Kramers behavior within the accessible temperature range, with indications of weak antiferromagnetic interactions and no detected long-range ordering. The significance of this magnetic platform lies in combining a triangular arrangement of Tm^{2+} moments with the distinct valence and coordination chemistry of a divalent ion. Although collective behavior remains unresolved, these features motivate further subkelvin quantum magnetic and thermodynamic studies and broaden the chemical options for designing rare-earth frustrated magnets.

The optical and electrical results extend the investigation of Tm^{2+} beyond its established use as a luminescent dopant. Alongside the characteristic near-infrared 4f−4f transition, low-lying $4f^{12}5d^1$ states provide broad visible−near-infrared absorption. Relative to dilute SrI_2:Tm^{2+} and structurally isolated Cs_4TmI_6, TmI_2 exhibits weaker detected emission but a more pronounced light-induced current. Photoinduced heating at both 690 and 808 nm further illustrates the excitation range accessible through the broad 4f−5d absorption envelope, beyond individual narrow Tm^{3+} 4f−4f bands. Together with thermally activated dark transport, these observations establish a range of photoresponses in a highly resistive Tm^{2+} solid, without requiring efficient luminescence.

The layered Tm−I framework adds intersite connectivity to the local coordination environment as a variable governing the electronic structure. Compared with the isolated octahedra in Cs_4TmI_6, the connected layers in TmI_2 exhibit greater calculated dispersion of the Tm 5d-derived states, while the occupied 4f-derived states remain highly localized. This contrast highlights the structural responsiveness of the optically accessible 5d manifold alongside the persistence of localized 4f character. The combination of this electronic structure with a measurable light-induced current makes extended Tm^{2+} frameworks relevant to the exploration of electrical as well as radiative responses to optical excitation.

These findings suggest complementary directions for Tm^{2+}-based materials design: dilution and local coordination can be explored to tune emission, while framework connectivity provides an additional variable for developing photoresponsive solids. The coexistence of low-lying $4f^{13}$ and $4f^{12}5d^1$ excited states also offers opportunities to examine how their relative energies influence competing relaxation pathways. The distinctive contribution of TmI_2 is the realization of a triangular lattice of $4f^{13}$ Kramers ions, accessible 4f−4f and 4f−5d excitations, and semiconductor-like transport with a reproducible light-induced electrical response within one layered divalent halide. This combination provides a chemically distinct foundation for exploring magnetic lattices and low-energy photoresponses within the same rare-earth framework.

3. CONCLUSION

This work establishes layered TmI_2 as a divalent rare-earth halide combining localized $4f^{13}$ Kramers magnetism with low-energy optical excitations and semiconductor-like electrical transport. Its triangular Tm^{2+} lattice exhibits predominantly single-ion magnetic behavior, indications of weak antiferromagnetic interactions, and no detected long-range ordering within the measured temperature range. Comparisons with Cs_4TmI_6 and SrI_2:Tm^{2+} reveal that TmI_2 retains both 4f−4f and 4f−5d optical channels while exhibiting weak luminescence, photoinduced heating at multiple excitation wave-

Downloaded from pubs.acs.org/jacsat/article-pdf/148/45/49310/6911201 8/jacs.6c15247.pdf by NANJING UNIV user on 19 November 2026

https://doi.org/10.1021/jacs.6c15247
J. Am. Chem. Soc. 2026, 148, 49310−49323

lengths, and a reproducible light-induced current despite its high resistivity. These findings extend the investigation of Tm^{2+} from localized luminescent centers to an extended solid hosting complementary magnetic, thermal, and electrical responses.

The combination realized in TmI_2 motivates both subkelvin studies of its magnetic ground state and further exploration of framework connectivity as a variable in rare-earth photoresponsive materials. Beyond Tm^{2+}, Dy^{2+}- and Nd^{2+}-containing solids in which $4f^{10}$ and $4f^4$ configurations are stabilized offer candidates for investigating how localized magnetic degrees of freedom coexist with low-lying 5d-derived optical excitations. Controlling the relative energies and spatial character of these states through coordination and lattice design could broaden the range of low-valent rare-earth solids available for integrating magnetic and photoresponsive functions.

■ ASSOCIATED CONTENT

Supporting Information

The Supporting Information is available free of charge at https://pubs.acs.org/doi/10.1021/jacs.6c15247.

Experimental section, structural characterization data, composition and morphology characterizations, spectroscopic characterizations, theoretical calculations, physical property measurements, and the corresponding data analyses (PDF)

Accession Codes

Deposition Numbers 2560462 and 2560531 contain the supplementary crystallographic data for this paper. These data can be obtained free of charge via the joint Cambridge Crystallographic Data Centre (CCDC) and Fachinformationszentrum Karlsruhe Access Structures service.

■ AUTHOR INFORMATION

Corresponding Authors

Zhaobo Hu − *School of Chemistry and Chemical Engineering, Jiangxi Provincial Key Laboratory of Functional Crystalline Materials Chemistry, Jiangxi University of Science and Technology, Ganzhou 341000, China;* orcid.org/0000-0001-9266-6624; Email: huzhaobo@smail.nju.edu.cn

Shuang Chen − *Kuang Yaming Honors School, Nanjing University, Nanjing 210023, China;* orcid.org/0000-0003-1334-2213; Email: chenshuang@nju.edu.cn

Ningxin Jiang − *State Key Laboratory of Coordination Chemistry, School of Chemistry, Nanjing University, Nanjing 210023, China;* orcid.org/0000-0001-7055-9334; Email: njiang@nju.edu.cn

Authors

Hao Ni − *State Key Laboratory of Coordination Chemistry, School of Chemistry, Nanjing University, Nanjing 210023, China*

Mingyang Yuan − *State Key Laboratory of Coordination Chemistry, School of Chemistry, Nanjing University, Nanjing 210023, China*

Lin-Ke Li − *National Laboratory of Solid State Microstructures and Department of Physics and Kuang Yaming Honors School, Nanjing University, Nanjing, Jiangsu 210023, China*

Zhe Wang − *State Key Laboratory of Coordination Chemistry, School of Chemistry, Nanjing University, Nanjing 210023, China*

Lili Zhao − *State Key Laboratory of Analytical Chemistry for Life Science, Key Laboratory of Mesoscopic Chemistry of MOE, School of Chemistry, Nanjing University, Nanjing 210023, China*

Zhengwei Fu − *State Key Laboratory of Analytical Chemistry for Life Science, Key Laboratory of Mesoscopic Chemistry of MOE, School of Chemistry, Nanjing University, Nanjing 210023, China*

Yue Zhao − *State Key Laboratory of Coordination Chemistry, School of Chemistry, Nanjing University, Nanjing 210023, China;* orcid.org/0000-0001-6094-4087

Song Bao − *National Laboratory of Solid State Microstructures and Department of Physics, Collaborative Innovation Center of Advanced Microstructures and Jiangsu Physical Science Research Center, Nanjing University, Nanjing 210023, China;* orcid.org/0000-0002-6241-7712

Weigao Xu − *State Key Laboratory of Analytical Chemistry for Life Science, Key Laboratory of Mesoscopic Chemistry of MOE, School of Chemistry, Nanjing University, Nanjing 210023, China;* orcid.org/0000-0002-3014-756X

Qiuxiang Wang − *Instrumental Analysis Center, Huaqiao University, Xiamen 361021, China;* orcid.org/0000-0002-4657-5331

Jinsheng Wen − *National Laboratory of Solid State Microstructures and Department of Physics, Collaborative Innovation Center of Advanced Microstructures and Jiangsu Physical Science Research Center, Nanjing University, Nanjing 210023, China;* orcid.org/0000-0001-5864-1466

Complete contact information is available at: https://pubs.acs.org/10.1021/jacs.6c15247

Funding

This work was supported by startup funds provided by Nanjing University and by the National Natural Science Foundation of China (U25A20567), the Natural Science Foundation of Jiangxi Province (20252BAC220020), and the Fundamental and Interdisciplinary Disciplines Breakthrough Plan of the Ministry of Education of China (JYB2025XDXM309). We also acknowledge support from the State Key Laboratory of Coordination Chemistry.

Notes

The authors declare no competing financial interest.

■ ACKNOWLEDGMENTS

The computation was performed in the High-Performance Computing Center (HPCC) and the High-Performance Computing Center of the Collaborative Innovation Center of Advanced Microstructures in Nanjing University. We thank Xuliang Lu and Prof. Deju Ye for providing access to the photothermal measurement setup and for guidance with the measurements. We are grateful to Prof. You Song, Prof. Youxuan Zheng, Prof. Jing Ma, and Prof. Shangshang Chen for helpful discussions.

■ REFERENCES

(1) Yan, C.-H.; Huang, X. Review on progress of rare earth science and technology in 2024. *J. Rare Earths* **2025**, *43* (10), 2029−2052.

Downloaded from pubs.acs.org/jacsat/article-pdf/148/45/49310/6911201 8/jacs.6c15247.pdf by NANJING UNIV user on 19 November 2026

(2) Su, P.; Song, F.; Cao, J.; Yan, C.-H.; Tang, Y. Rare earth complex-based functional materials: from molecular design and performance regulation to unique applications. *Acc. Chem. Res.* **2025**, *58* (2), 218−230.
(3) Atwood, D. A. *rare earth elements: fundamentals and applications.*; John Wiley & Sons, 2013.
(4) Song, F.-J.; Su, P.; Li, X.; Yan, C.-H.; Zhang, J.-L.; Tang, Y. Harnessing rare earth coordination chemistry for advanced photo-functional materials: from fundamental principles to emerging technologies. *Chem. Soc. Rev.* **2026**, *55* (9), 5117−5197.
(5) Thiel, C. W.; Böttger, T.; Cone, R. Rare-earth-doped materials for applications in quantum information storage and signal processing. *J. Lumin* **2011**, *131* (3), 353−361.
(6) Pisarski, W. A. Rare earth doped glasses/ceramics: Synthesis, structure, properties and their optical applications. *Materials* **2022**, *15* (22), 8099.
(7) Zeng, Z.; Xu, Y.; Zhang, Z.; Gao, Z.; Luo, M.; Yin, Z.; Zhang, C.; Xu, J.; Huang, B.; Luo, F.; Du, Y. Rare-earth-containing perovskite nanomaterials: design, synthesis, properties and applications. *Chem. Soc. Rev.* **2020**, *49* (4), 1109−1143.
(8) Boggiano, A. C.; Studvick, C. M.; Roy Chowdhury, S.; Niklas, J. E.; Tateyama, H.; Wu, H.; Leisen, J. E.; Kleemiss, F.; Vlaisavljevich, B.; Popov, I. A.; La Pierre, H. S. Praseodymium in the formal + 5 oxidation state. *Nat. Chem.* **2025**, *17* (7), 1005−1010.
(9) Ramanathan, A.; Kaplan, J.; Sergentu, D.-C.; Branson, J. A.; Ozerov, M.; Kolesnikov, A. I.; Minasian, S. G.; Autschbach, J.; Freeland, J. W.; Jiang, Z.; Mourigal, M. Chemical design of electronic and magnetic energy scales of tetravalent praseodymium materials. *Nat. Commun.* **2023**, *14* (1), 3134.
(10) Palumbo, C. T.; Zivkovic, I.; Scopelliti, R.; Mazzanti, M. Molecular complex of Tb in the + 4 oxidation state. *J. Am. Chem. Soc.* **2019**, *141* (25), 9827−9831.
(11) Zhang, Q.; Hu, S. X.; Qu, H.; Su, J.; Wang, G.; Lu, J. B.; Chen, M.; Zhou, M.; Li, J. Pentavalent lanthanide compounds: formation and characterization of praseodymium(V) oxides. *Angew. Chem., Int. Ed.* **2016**, *128* (24), 7010−7014.
(12) Gompa, T. P.; Ramanathan, A.; Rice, N. T.; La Pierre, H. S. The chemical and physical properties of tetravalent lanthanides: Pr, Nd, Tb, and Dy. *Dalton Trans.* **2020**, *49* (45), 15945−15987.
(13) Montini, T.; Melchionna, M.; Monai, M.; Fornasiero, P. Fundamentals and catalytic applications of CeO_2-based materials. *Chem. Rev.* **2016**, *116* (10), 5987−6041.
(14) Wedal, J. C.; Evans, W. J. A rare-earth metal retrospective to stimulate all fields. *J. Am. Chem. Soc.* **2021**, *143* (44), 18354−18367.
(15) Meyer, G. Reduced halides of the rare-earth elements. *Chem. Rev.* **1988**, *88* (1), 93−107.
(16) Flahaut, J. Sulfides, selenides and tellurides. *Handb. Phys. Chem. Rare Earths* **1979**, *4*, 1−88.
(17) MacDonald, M. R.; Bates, J. E.; Ziller, J. W.; Furche, F.; Evans, W. J. Completing the series of + 2 ions for the lanthanide elements: synthesis of molecular complexes of Pr^{2+}, Gd^{2+}, Tb^{2+}, and Lu^{2+}. *J. Am. Chem. Soc.* **2013**, *135* (26), 9857−9868.
(18) Gould, C. A.; McClain, K. R.; Yu, J. M.; Groshens, T. J.; Furche, F.; Harvey, B. G.; Long, J. R. Synthesis and magnetism of neutral, linear metallocene complexes of terbium(II) and dysprosium(II). *J. Am. Chem. Soc.* **2019**, *141* (33), 12967−12973.
(19) Gould, C. A.; McClain, K. R.; Reta, D.; Kragskow, J. G.; Marchiori, D. A.; Lachman, E.; Choi, E.-S.; Analytis, J. G.; Britt, R. D.; Chilton, N. F.; Harvey, B. G. Ultrahard magnetism from mixed-valence dilanthanide complexes with metal-metal bonding. *Science* **2022**, *375* (6577), 198−202.
(20) Liu, M.; Chen, Y.-C.; Wang, H.; Shang, T.; Tong, M.-L.; Layfield, R. A.; Mansikkamäki, A.; Guo, F.-S. A linear dysprosium (II) metallocene with a high effective energy barrier and magnetic hysteresis up to 70 K. *J. Am. Chem. Soc.* **2025**, *147* (21), 18307−18316.
(21) Luevano, M. R.; Stennett, C. R.; Ma, E.; Ziller, J. W.; Furche, F.; Evans, W. J. The Divergent Reduction Chemistry of Ln(II) Bis (terphenylthiolate) Complexes, Ln $(SAr^{iPr6})_2$, Leads to KLn (μ-$SAr^{iPr6})_2$, C— H Bond Activation Products, and Two-Electron Reduction Reactivity. *J. Am. Chem. Soc.* **2025**, *147* (38), 34249−34255.
(22) Meyer, G. Small cause−Great effect: What the $4f^{n+1}d^0 \rightarrow 4f^nd^1$ configuration crossover does to the chemistry of divalent rare-earth halides and coordination compounds. *J. Solid State Chem.* **2019**, *270*, 324−334.
(23) Suta, M.; Wickleder, C. Synthesis, spectroscopic properties and applications of divalent lanthanides apart from Eu^{2+}. *J. Lumin* **2019**, *210*, 210−238.
(24) Xémard, M.; Jaoul, A.; Cordier, M.; Molton, F.; Cador, O.; Le Guennic, B.; Duboc, C.; Maury, O.; Clavaguéra, C.; Nocton, G. Divalent thulium triflate: a structural and spectroscopic study. *Angew. Chem., Int. Ed.* **2017**, *129* (15), 4330−4335.
(25) Jaroschik, F.; Nief, F.; Le Goff, X.-F.; Ricard, L. Synthesis and reactivity of organometallic complexes of divalent thulium with cyclopentadienyl and phospholyl ligands. *Organometallics* **2007**, *26* (14), 3552−3558.
(26) Asprey, L.; Kruse, F. Thulium di-iodide. *J. Inorg. Nucl. Chem.* **1960**, *13* (1−2), 32−35.
(27) Matthias, B.; Bozorth, R.; Van Vleck, J. Ferromagnetic interaction in EuO. *Phys. Rev. Lett.* **1961**, *7* (5), 160.
(28) Boulon, G. Why so deep research on Yb^{3+}-doped optical inorganic materials? *J. Alloy. Compd.* **2008**, *451* (1−2), 1−11.
(29) Paddison, J. A.; Daum, M.; Dun, Z.; Ehlers, G.; Liu, Y.; Stone, M. B.; Zhou, H.; Mourigal, M. Continuous excitations of the triangular-lattice quantum spin liquid $YbMgGaO_4$. *Nat. Phys.* **2017**, *13* (2), 117−122.
(30) Shen, Y.; Li, Y.-D.; Wo, H.; Li, Y.; Shen, S.; Pan, B.; Wang, Q.; Walker, H.; Steffens, P.; Boehm, M.; Hao, Y.; et al. Evidence for a spinon Fermi surface in a triangular-lattice quantum-spin-liquid candidate. *Nature* **2016**, *540* (7634), 559−562.
(31) Plokker, M.; Hoogsteen, W.; Abellon, R.; Krämer, K.; van der Kolk, E. Concentration and temperature dependent luminescence properties of the SrI_2-TmI_2 system. *J. Lumin.* **2020**, *225*, 117327.
(32) Miller, G.; Smith, M.; Wang, M.; Wang, S. The synthesis and crystal structure of Rb_4TmI_6: Lattice energy calculations on networks of condensed cubes. *J. Alloy. Compd.* **1998**, *265* (1), 140−145.
(33) Wang, Z.; Ni, H.; Yuan, M.; Fang, X.; Peng, X.; Zhao, Y.; Jiang, N. ZnI_2-Mediated Synthesis of High-Purity Rare Earth Iodides with Systematic UV−Vis−NIR Absorption Signatures. *Inorg. Chem.* **2026**, *65* (20), 11044−11052.
(34) Fieser, M. E.; MacDonald, M. R.; Krull, B. T.; Bates, J. E.; Ziller, J. W.; Furche, F.; Evans, W. J. Structural, spectroscopic, and theoretical comparison of traditional vs recently discovered Ln^{2+} ions in the [K (2.2.2-cryptand)][$(C_5H_4SiMe_3)_3Ln$] complexes: the variable nature of Dy^{2+} and Nd^{2+}. *J. Am. Chem. Soc.* **2015**, *137* (1), 369−382.
(35) Lawson, K.; Wallbridge, S. P.; Catling, A. E.; Kirk, C. A.; Dann, S. E. Determination of layered nickel hydroxide phases in materials disordered by stacking faults and interstratification. *J. Mater. Chem. A* **2023**, *11* (2), 789−799.
(36) Sławiński, W. A.; Sjåstad, A. O.; Fjellvåg, H. Stacking Faults and Polytypes for Layered Double Hydroxides: What Can We Learn from Simulated and Experimental X-ray Powder Diffraction Data? *Inorg. Chem.* **2016**, *55* (24), 12881−12889.
(37) Gruber, J. B.; Hills, M. E.; Macfarlane, R. M.; Morrison, C. A.; Turner, G. A.; Quarles, G. J.; Kintz, G. J.; Esterowitz, L. Spectra and energy levels of Tm^{3+}: $Y_3Al_5O_{12}$. *Phys. Rev. B* **1989**, *40* (14), 9464.
(38) De Jong, M.; Meijerink, A.; Seijo, L.; Barandiarán, Z. Energy level structure and multiple $4f^{12}d^1$ emission bands for Tm^{2+} in halide perovskites: theory and experiment. *J. Phys. Chem. C* **2017**, *121* (18), 10095−10101.
(39) Plokker, M. P.; Vlaar, S.; Bakx, A. H.; van der Kolk, E.; Dorenbos, P.; Hintzen, H. T. Evaluating the Tm^{2+} $4f^{12}d^1 \rightarrow 4f^{13}$ and $4f^{13} \rightarrow 4f^{13}$ luminescence and quenching dynamics in orthorhombic $BaCl_2$. *J. Phys. Chem. C* **2023**, *127* (38), 19017−19026.
(40) Rogers, E.; Dorenbos, P.; De Haas, J.; Van Der Kolk, E. Experimental study of the $4f^n \rightarrow 4f^n$ and $4f^n \rightarrow 4f^{n-1}d^1$ transitions of

Downloaded from pubs.acs.org/jacsat/article-pdf/148/45/49310/6911201 8/jacs.6c15247.pdf by NANJING UNIV user on 19 November 2026

https://doi.org/10.1021/jacs.6c15247
J. Am. Chem. Soc. 2026, 148, 49310−49323

the lanthanide diiodides LnI_2 (Ln= Nd, Sm, Eu, Dy, Tm, Yb). *J. Phys.: Condens. Matter* **2012**, *24* (27), 275502.
(41) Nath, K. G.; Ufuktepe, Y.; Kimura, S.; Kinoshita, T.; Kumigashira, H.; Takahashi, T.; Matsumura, T.; Suzuki, T.; Ogasawara, H.; Kotani, A. 4d Core-level resonant photoemission spectroscopy of thulium monochalcogenides around the Tm3d threshold. *J. Electron Spectrosc. Relat. Phenom.* **1998**, *88*, 369−375.
(42) Gołacki, Z.; Heinonen, M. Valency of Yb in PbS and PbTe determined by XPS. *Acta Phys. Pol., A* **1997**, *91* (4), 775−778.
(43) Hsu, Y.-L.; Li, C.; Jones, A. C.; Pettes, M. T.; Chowdhury, A.; Yan, Y.; Yoon, H. P. Subsurface Characteristics of Metal-Halide Perovskites Polished by an Argon Ion Beam. *J. Phys. Chem. C* **2023**, *127* (15), 7461−7470.
(44) Usman, T.; Khan, S.; Khan, D. F.; Murtaza, G.; Khan, M. Y. Tailoring halide perovskite materials $CsTmX_3$ (X= F, Cl, Br, I) for enhanced optoelectronic and thermoelectric characteristics through first-principles investigations. *Int. J. Mod. Phys. B* **2026**, *40* (11), 2650088.
(45) Bordelon, M. M.; Kenney, E.; Liu, C.; Hogan, T.; Posthuma, L.; Kavand, M.; Lyu, Y.; Sherwin, M.; Butch, N. P.; Brown, C.; et al. Field-tunable quantum disordered ground state in the triangular-lattice antiferromagnet $NaYbO_2$. *Nat. Phys.* **2019**, *15* (10), 1058−1064.
(46) Ma, Z.; Wang, J.; Dong, Z.-Y.; Zhang, J.; Li, S.; Zheng, S.-H.; Yu, Y.; Wang, W.; Che, L.; Ran, K.; et al. Spin-glass ground state in a triangular-lattice compound $YbZnGaO_4$. *Phys. Rev. Lett.* **2018**, *120* (8), 087201.
(47) Moutet, J.; Schleinitz, J.; La Droitte, L.; Tricoire, M.; Pointillart, F.; Gendron, F.; Simler, T.; Clavaguéra, C.; Le Guennic, B.; Cador, O.; et al. Bis-Cyclooctatetraenyl Thulium(II): Highly Reducing Lanthanide Sandwich Single-Molecule Magnets. *Angew. Chem., Int. Ed.* **2021**, *133* (11), 6107−6111.
(48) Suryanarayanan, R.; Güntherodt, G.; Freeouf, J.; Holtzberg, F. Optical and photoemission studies of TmTe. *Phys. Rev. B* **1975**, *12* (10), 4215.
(49) Bucher, E.; Andres, K.; Di Salvo, F.; Maita, J.; Gossard, A.; Cooper, A.; Hull, G., Jr Magnetic and some thermal properties of chalcogenides of Pr and Tm and a few other rare earths. *Phys. Rev. B* **1975**, *11* (1), 500.
(50) Dissanayaka Mudiyanselage, R. S.; Wang, H.; Vilella, O.; Mourigal, M.; Kotliar, G.; Xie, W. $LiYbSe_2$: Frustrated Magnetism in the Pyrochlore Lattice. *J. Am. Chem. Soc.* **2022**, *144* (27), 11933−11937.
(51) Li, Y.; Liao, H.; Zhang, Z.; Li, S.; Jin, F.; Ling, L.; Zhang, L.; Zou, Y.; Pi, L.; Yang, Z.; et al. Gapless quantum spin liquid ground state in the two-dimensional spin-1/2 triangular antiferromagnet $YbMgGaO_4$. *Sci. Rep.* **2015**, *5* (1), 16419.
(52) Pan, B. L.; Ni, J. M.; He, L. P.; Yu, Y. J.; Xu, Y.; Li, S. Y. Specific heat and thermal conductivity of the triangular-lattice rare-earth material $KBaYb(BO_3)_2$ at ultralow temperature. *Phys. Rev. B* **2021**, *103* (10), 104412.
(53) Tokiwa, Y.; Bachus, S.; Kavita, K.; Jesche, A.; Tsirlin, A. A.; Gegenwart, P. Frustrated magnet for adiabatic demagnetization cooling to milli-Kelvin temperatures. *Commun. Mater.* **2021**, *2* (1), 42.
(54) Xu, Q.-F.; Wu, R.-T.; Long, L.-S.; Zheng, L.-S. Ultralow-Temperature Magnetic Refrigeration Inorganic Materials: From Designed Synthesis to Adiabatic Demagnetization Refrigeration. *Acc. Chem. Res.* **2025**, *58* (18), 2898−2909.
(55) Patil, A. S.; Patil, A. V.; Dighavkar, C. G.; Adole, V. A.; Tupe, U. J. Synthesis techniques and applications of rare earth metal oxides semiconductors: A review. *Chem. Phys. Lett.* **2022**, *796*, 139555.
(56) Joos, J. J.; Korthout, K.; Amidani, L.; Glatzel, P.; Poelman, D.; Smet, P. F. Identification of Dy^{3+}/Dy^{2+} as Electron Trap in Persistent Phosphors. *Phys. Rev. Lett.* **2020**, *125* (3), 033001.
(57) Nexha, A.; Pujol, M. C.; Carvajal, J. J.; Díaz, F.; Aguiló, M. Effect of the Size and Shape of Ho, Tm: $KLu(WO4)_2$ Nanoparticles on Their Self-Assessed Photothermal Properties. *Nanomaterials* **2021**, *11* (2), 485.
(58) Nexha, A.; Lu, D.; Pujol, M. C.; Massons, J.; Haro Gonzales, P.; Serier-Brault, H.; Carvajal, J. J. 808 nm near infrared excited Ho^{3+} and Tm^{3+} based metal−organic frameworks for luminescence thermometry and photothermal conversion. *Dalton Trans.* **2025**, *54* (40), 15271−15280.
(59) Yu, X.-Q.; Sun, C.; Liu, B.-W.; Wang, M.-S.; Guo, G.-C. Directed self-assembly of viologen-based 2D semiconductors with intrinsic UV−SWIR photoresponse after photo/thermo activation. *Nat. Commu.n* **2020**, *11* (1), 1179.

Downloaded from pubs.acs.org/jacsat/article-pdf/148/45/49310/6911201 8/jacs.6c15247.pdf by NANJING UNIV user on 19 November 2026

https://doi.org/10.1021/jacs.6c15247
J. Am. Chem. Soc. 2026, 148, 49310−49323